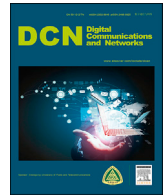




Contents lists available at ScienceDirect

Digital Communications and Networks

journal homepage: www.keaipublishing.com/dcan

Submillimeter wave communication versus millimeter wave communication

Madhuprana Goswami^{*}, Hyuck M. Kwon

Department of Electrical Engineering and Computer Science, Wichita State University, 1845 N. Fairmount, Wichita, KS, 67260, USA

ARTICLE INFO

Keywords:

Submillimeter wave antenna
 Millimeter wave antenna
 Rectangular micro-strip patch antenna
 Cylindrical dielectric resonator antenna
 Massive submillimeter wave MIMO antenna
 Applications

ABSTRACT

This paper studies the performance of a submillimeter wave antenna operating between frequencies 0.1 THz and 10 THz with a 4-cyano-4-pentylbiphenyl [5CB] substrate. Since the size and shape of the antenna impact its gain/directivity, resonant frequency, bandwidth, and efficiency, the two antenna types considered in this paper are: (a) Rectangular Patch Antenna (RPA), and (b) Cylindrical Dielectric Resonator Antenna (CDRA). Here a submillimeter wave antenna is compared with a millimeter wave (a few GHz to 100 GHz) antenna. These popular mm-wave antennas are chosen for the submillimeter wave antenna in order to understand changes in their performance as the result of changes in their geometrical shape. FEldberechnung bei Körpern mit beliebiger Oberfläche (FEKO) software is used for the design and calculation of the Three-Dimensional (3D) ElectroMagnetic (EM) patterns. This paper also concentrates on the design and analysis of a massive submillimeter wave Multiple-Input Multiple-Output (MIMO) (8 by 8) RPA and CDRA.

1. Introduction

The increasing demand for Multiple-Input Multiple-Output (MIMO) communication technology has motivated this work. Since communication devices operating at high frequencies are studied extensively [1, 2], this paper uses submillimeter wave frequency band and observes the behavior of massive MIMO antennas in that band. At the same time, the behavior of the antenna operating over a millimeter wave frequency band is compared in this paper. A perfect electric conductor is used in designing the MIMO antenna. The 4-cyano-4-pentylbiphenyl (5CB) nematic liquid crystal with a dielectric constant of 8.58 [3,4,5] is chosen as the substrate mainly because of its behavior as a dipole, with both positive and negative polarities in the presence of external magnetic and electric fields, as described in detail in Ref. [6]. In addition, the massive MIMO technology (also known as large-scale antenna systems) basically uses a very large number of service antennas (e.g., hundreds or thousands) that are operated fully coherently and adaptively [7,8,9,10,11]. Extra antennas help by focusing the transmission and reception of the signal energy into ever-smaller regions of space. This can result in huge improvements in throughput and energy efficiency, particularly when combined with the simultaneous scheduling of a large number of user terminals (e.g., tens or hundreds), as explained in Refs. [7,8,9,10,11]. Submillimeter wave massive MIMO can help to improve antenna efficiency by deploying an array of low-power, low-cost miniature

antennas. Simulations in this paper are performed using the real part of the complex dielectric constant of 5CB liquid crystal droplets as the antenna substrate.

This paper introduces, for the first time, a submillimeter wave massive MIMO antenna design. It also shows that with digital Beam-Forming (BF), one can compensate the path loss due to the high frequency range of a submillimeter wave and hence increase the gain for a submillimeter wave massive MIMO antenna. For the first time in this paper, performances of the massive MIMO Rectangular Patch Antenna (RPA) and massive MIMO Cylindrical Dielectric Resonator Antenna (CDRA) operating over a submillimeter wave frequency band are compared with their performances over a millimeter wave frequency band. Figs. 1 and 2 show the antenna designs, respectively, for a massive 64-element MIMO RPA and a massive 64-element MIMO CDRA with an operating frequency over the submillimeter wave frequency band.

This paper is organized as follows: Section 2 performs theoretical analysis for both antenna types (RPA and CDRA) used in this paper. Section 3 explains the parameters used for designing the antenna using FEldberechnung bei Körpern mit beliebiger Oberfläche (FEKO) and the simulated results. It also draws comparisons between the millimeter wave antenna and the submillimeter wave antenna. Section 4 presents the massive submillimeter wave MIMO antenna design and an analysis, and also compares the simulated results with that of the millimeter wave massive MIMO antenna. Section 5 offers the conclusions.

^{*} Corresponding author.

E-mail addresses: mxgoswami@shockers.wichita.edu (M. Goswami), hyuck.kwon@wichita.edu (H.M. Kwon).

<https://doi.org/10.1016/j.dcan.2019.04.002>

Received 26 June 2017; Received in revised form 13 April 2019; Accepted 16 April 2019

Available online xxx

2352-8648/© 2019 Chongqing University of Posts and Telecommunications. Production and hosting by Elsevier B.V. This is an open access article under the CC BY-

NC-ND license (<http://creativecommons.org/licenses/by-nc-nd/4.0/>).

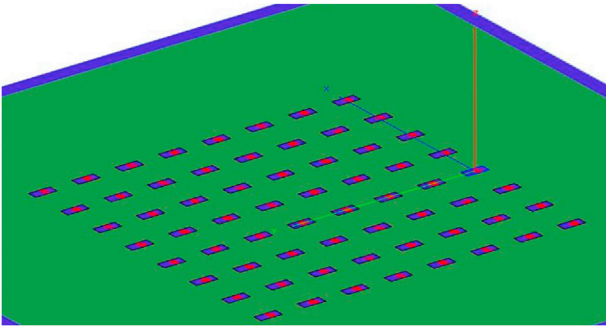


Fig. 1. 8×8 massive submillimeter MIMO rectangular patch antenna model.

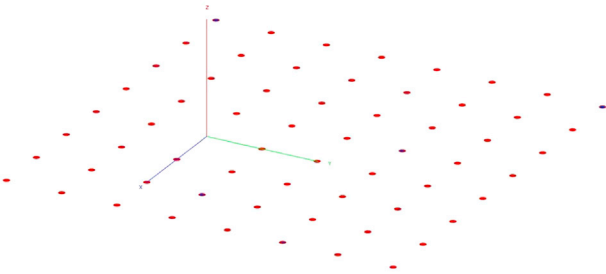


Fig. 2. 8×8 massive submillimeter MIMO cylindrical dielectric resonator antenna model.

2. Antenna design and theoretical analysis

The antenna design and analysis method employed in this paper is the Method of Moments (MoM), as it is the core of the program upon which FEKO is based [12]. In this section, we analyze the basic features of RPA and CDRA based on the commonly known antenna designing procedures in Refs. [13,14]. The basic difference between the CDRA and RPA is obviously the shape. The CDRA is characterized by its height and radius, while the RPA is characterized by a rectangular patch length, patch width, dielectric substrate height and resonant impedance. Also, this paper considers the case that the CDRA is excited using a probe feeding method [14] while the RPA is excited using a pin feeding method [13]. Since both antenna models are widely utilized, this section clearly cites all major equations for theoretically analyzing the differences between the two models.

2.1. Rectangular patch antenna

The rectangular patch is one of the most widely used antenna configurations. In this paper, the rectangular patch antenna is modelled using a pin-feeding method. The dielectric substrate is modelled as a planar multilayer substrate with a bottom ground layer using the special Greens function. The dielectric substrate used for designing the millimeter wave RPA is RT/duroid 5880 with a dielectric constant of 2.2, while the dielectric substrate for the submillimeter wave RPA is 5CB liquid crystal droplets with a dielectric constant of 8.58. An infinite ground plane is used to reduce the simulation time but may not be an exact representation of a physical antenna. The operating frequency of the millimeter wave antenna is taken as 3–100 GHz, while that of the submillimeter wave antenna is taken as 0.1–10 THz. The resonant frequencies of both antennas are obtained from eqn. 14–33 in Ref. [13].

Once the input parameters, substrate height, resonant impedance and dielectric constant are chosen for the effective antenna design, it is necessary to calculate the Width (W) and the Length (L) of the patch. The input parameters for designing the RPA at the millimeter wave are chosen from example 14.1 in Ref. [13]; while for designing the RPA at the submillimeter wave, we choose a considerably small substrate height of

2805 nm and a resonant impedance of 50 ohm. The width of the patch is calculated using the standard eqn. 14-6 stated in Ref. [13]. The effective dielectric constant is ϵ_{reff} and can be written using eqn. 14-1 in Ref. [13]. The actual physical length of the patch can also be calculated using eqn. 14-7 in Ref. [13]. Finally, the effective length of the patch for the dominant transverse electromagnetic TM_{010}^x mode with no fringing effect can be calculated from eqn. 14-3 in Ref. [13].

The next task is to calculate the parallel equivalent admittance for the radiating patch. The equivalent admittance is expressed in terms of the conductance and the susceptance. The conductance of a uniform radiating slot is obtained from eqns. 14-10, 14-11, 14-12, and 14-12a in Ref. [13]. In Ref. [13], θ is the polar angle in the spherical coordinate system used for antenna analysis, and k_0 is the propagation factor, which is often known as the vector wave number. The mutual conductance between the non-uniform radiating slots of the patch antenna is calculated according to eqn. 14-18a in Ref. [13] as well. Finally, the inset feed point distance y_0 is obtained using eqn. 14-20a in Ref. [13].

The MoM analysis method used in FEKO depends on the position of the feed, and hence the measured E-plane and H-plane patterns of the RPA are different from that of the computed pattern using MoM. This difference occurs in the computation because the position of the feed as calculated is not completely symmetrical along the E-plane [13]. Another very important antenna property is antenna directivity, which has been defined in Ref. [13] as the radiation intensity averaged over all directions, where the average radiation intensity is equal to the total power radiated by the antenna divided by 4π . The directivity of a rectangular patch antenna can be expressed using eqn. 14–50 in Ref. [13]. The next important antenna property that needs to be calculated is the quality factor.

As defined in eqn. 14–83 in Ref. [13], the quality factor Q_t can be expressed in terms of radiation, conduction, dielectric, and surface wave losses. Q_{rad} is the quality factor due to radiation losses, Q_c is the quality factor due to conduction losses, Q_d is the quality factor due to dielectric losses, and Q_{sw} is the quality factor due to the surface wave. The quality factor can be easily calculated from the fractional bandwidth of the antenna because it is inversely proportional to the quality factor and is defined accurately in eqn. 14-88a [13]. The total antenna efficiency e_0 is used to take into account the losses at the input terminals [5]. The total antenna efficiency can be expressed using eqn. 2–45 in Ref. [13], where e_{cd} is the antenna radiation efficiency, which is used to relate the gain and directivity, and $|\Gamma|$ is the magnitude of the reflection coefficient. The radiation efficiency of the rectangular patch antenna can be expressed in terms of a quality factor through eqn. 14–90 in Ref. [13]. The efficiency of the rectangular patch antenna varies with the substrate height and also with the dielectric constant of the substrate, which is to be discussed later in this paper. Another very useful measure describing the performance of an antenna is the gain, which is a measure that takes into account the efficiency of the antenna as well as its directional capabilities [13]. The gain expressed in terms of decibels is expressed through eqn. 2–52 in Ref. [13].

2.2. Cylindrical dielectric resonator antenna

The cylindrical dielectric resonator antenna has been used in circuit applications for several years [14]. The high Q factor and the compact size of these antennas make them ideal to be used in filters and oscillators [14]. The CDRA is characterized by its height H , radius a , and dielectric constant ϵ_r , and the aspect ratio $\frac{a}{H}$ determines the wave number $k_0 a$ and the Q factor for a given dielectric constant [14].

Different excitation modes of the CDRA can also be generated based on its aspect. If $0.33 \leq \frac{a}{H} \leq 5$, then mode $TE_{01\delta}$ and mode $TM_{01\delta}$ are valid; otherwise, if $0.4 \leq \frac{a}{H} \leq 6$, then mode HEM_{11} is valid [15]. The operating frequency of the millimeter wave CDRA is 3–100 GHz, and it varies for the submillimeter wave antenna between 0.1 and 10 THz. The CDRA is excited using probe feeding and analyzed using the pure MoM approach.

The dielectric constant of the substrate used for the CDRA at the millimeter wave is taken as 6.7, whereas 5CB droplets are used as the substrate of the CDRA at the submillimeter wave with a dielectric constant of 8.58. A set of reasonable input parameters for designing the CDRA at the millimeter wave are chosen from Table 2.5 in Ref. [14]. For the submillimeter wave CDRA design, we choose input parameters as follows: CDRA height as 0.05 nm, CDRA radius as 0.270 nm, and aspect ratio as 5.4. Since the operating frequency is very high, we consider considerably small radius and height for designing the submillimeter wave CDRA.

After the input parameters have been initialized, first the Q factor must be determined, which can be obtained from eqn. 2.12 for the $TE_{01\delta}$ excitation mode and eqn. 2.16 for the $HE_{11\delta}$ excitation mode in Ref. [14]. Then the dielectric constant of the substrate should be chosen, followed by calculation of the wave number k_0a . The wave number is expressed for the $TE_{01\delta}$ excitation mode through eqn. 2.11 and for the $HE_{11\delta}$ excitation mode through eqn. 2.15 in Ref. [14]. The radius of the CDRA can also be calculated if not initialized for a given aspect ratio and the calculated wave number. Once the Q factor has been calculated, the corresponding bandwidth is determined using eqn. 2.6 in Ref. [14]. The resonant frequency of the millimeter wave CDRA is taken to be 60 GHz, while the resonant frequency of the submillimeter wave CDRA is taken to be 10 THz. Depending on the aspect ratio, the excitation mode is determined. The millimeter wave CDRA has an aspect ratio of 3.56, and hence the $TE_{01\delta}$ mode is selected as the excitation mode, whereas the submillimeter wave CDRA has an aspect ratio of 5.4, and hence the HEM_{11} mode is selected as the excitation mode.

The total efficiency of the CDRA can be found by eqn. 2–45 in Ref. [13], where the radiation efficiency can be found by eqn. 10.3 in Ref. [14]. The antenna gain in eqn. 2–52 in Ref. [13] can be used to calculate the gain of the CDRA as well. The directivity of the CDRA is calculated by FEKO simulation, which will be tabulated later in this paper.

3. FEKO simulated results and analysis

3.1. Rectangular patch antenna

FEKO is an advanced 3D numerical electromagnetic simulator [16]. It helps to observe antenna patterns in 3D. Following the theoretical analysis described in the previous section, several approximations are made in order to simplify the computation for different antenna problems. The exact solutions to antenna problems are obtained numerically using FEKO. After simulation in FEKO, the output parameters of both the millimeter wave RPA and the submillimeter wave RPA are tabulated, as shown in Table 1, which helps to compare the two.

The submillimeter wave single-element RPA has been designed with a

Table 1
FEKO simulated output parameters of RPA.

Output parameter	Millimeter wave RPA	Submillimeter wave RPA
Patch width (W)	1.18 cm	2329.71 nm
Effective dielectric constant (ϵ_{eff})	1.97	5.67
Incremental length (ΔL)	0.081 cm	784.27 nm
Physical length (L)	0.90 cm	516.65 nm
Effective length (L_{eff})	1.06 cm	2085.20 nm
Inset feed point distance (y_0)	0.31 cm	-363.14 nm
Wavelength (λ)	2.13 cm	29,979 nm
Fractional bandwidth (BW)	0.034	0.43
Percentage bandwidth	3.47 percent	43.92 percent
Reflection coefficient magnitude ($ \Gamma $)	$0.85 \leq \Gamma \leq 0.96$	$0.71 \leq \Gamma \leq 0.97$
Quality factor (Q_c)	2.88	2.32
Maximum gain (G_0)	5.89 dBi	-8.87 dBi
Maximum efficiency (ϵ_0)	100 percent	82.97 percent

metallic rod as the conducting probe and 5CB liquid crystal droplets as the substrate. The Cole-Cole and Debye method is applied to find the complex dielectric constant of the 5CB liquid crystal in Ref. [17], and the complex dielectric constant is expressed in Ref. [18] as

$$\epsilon^*(\omega) = \epsilon_\infty + \frac{\epsilon_0 - \epsilon_\infty}{1 + (i\omega\tau)^{1-\alpha}} \quad (1)$$

where ϵ_0 is the limiting low-frequency dielectric constant, ϵ_∞ is the limiting high-frequency dielectric constant, τ is the average relaxation time, and α is the distribution parameter. The complex dielectric constant can also be expressed through [19] as

$$\epsilon^* = \epsilon' - j\epsilon'' \quad (2)$$

where ϵ' is the static dielectric constant and ϵ'' is the imaginary part of the complex dielectric constant. In Ref. [18], the values of ϵ' and ϵ'' for the 5CB liquid crystal droplets have been computed. The complex dielectric constant calculated using eqn. (2) is found to be 81.91 at an excitation voltage of 1 V. The calculated dielectric constant is a very high quantity, and hence when applied to the design in FEKO, the preprocessor of FEKO cannot compute all of the necessary integrations when MoM is used as the method of analysis. Hence, for maintaining the simplicity of computation, only the real part of the complex dielectric constant of the 5CB liquid crystal is used as the dielectric constant of the substrate for the submillimeter wave RPA and the submillimeter wave CDRA. The ϵ' as calculated in Ref. [19] is 8.58 for 1 V of excitation voltage, 8.28 for 2 V of excitation voltage, 18.49 for 12 V of excitation voltage, and 19.40 for 20 V of excitation voltage, respectively. The design in this paper applies 1 V of excitation voltage only; hence, the dielectric constant of the 5CB liquid crystal substrate is taken as 8.58. A perfect electric conductor is used for the MIMO antenna design. In a practical scenario, the excitation voltage may drift [20]; hence, we vary the excitation voltage (E) as 2 V and 5 V, and plot the RPA antenna pattern and gain over both the millimeter and submillimeter wave frequency bands. The excitation voltage at the antenna's feed point is a function of feed point impedance (Z) and the power received (P) by the antenna, and can be expressed as

$$E = \sqrt{ZP}. \quad (3)$$

Figs. 3 and 4 show the plots of the far-field radiation pattern and gain of the millimeter wave RPA when the excitation voltage is varied to 2 V and 5 V, while Figs. 5 and 6 show the same for the submillimeter wave RPA. It can be seen that the antenna gain increases with the increase in the excitation voltage. When the excitation voltage is 1 V, 2 V, and 5 V, the gain is 5.89 dBi, 6.60 dBi, and 7.03 dBi, respectively, in the case of the millimeter wave RPA. For an excitation voltage of 1 V, 2 V, and 5 V, the antenna gain is -8.87 dBi, -7.66 dBi, and -7.22 dBi, respectively. Due to space limitations, we performed this experiment only for the RPA.

Some of the ideal conditions in this paper have been used specially to simplify the calculation using FEKO. When we use some practical antenna parameters, such as the excitation modes of CDRA, other than

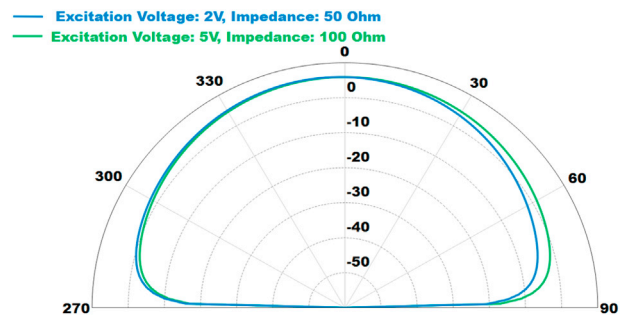


Fig. 3. Millimeter wave RPA: Far-field radiation patterns due to excitation voltage of 2 V, 5 V.

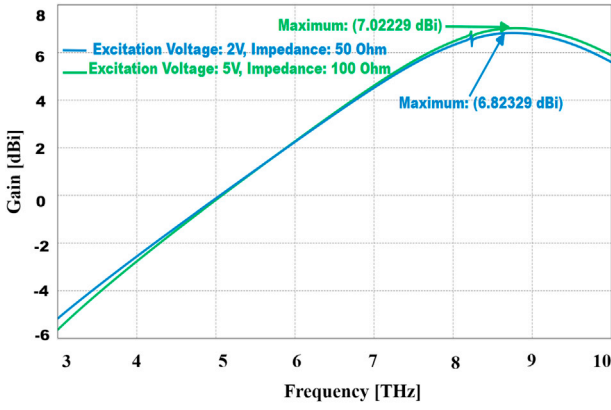


Fig. 4. Millimeter wave RPA: Antenna gains due to excitation voltage of 2 V, 5 V.

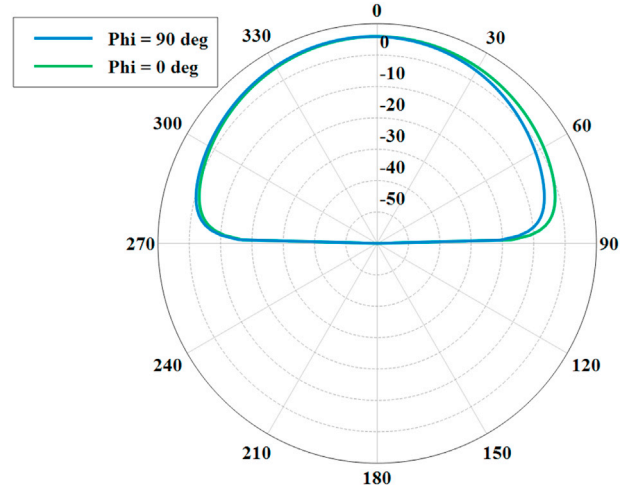


Fig. 7. Millimeter wave RPA: Far-field radiation patterns in E- and H- planes.

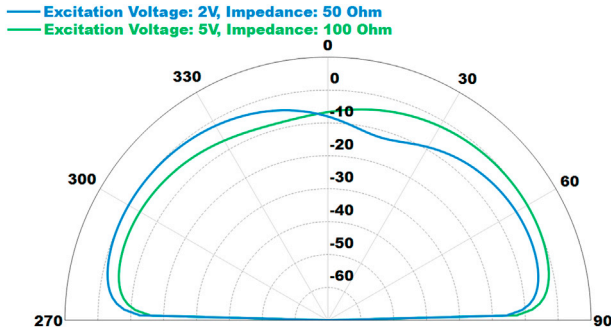
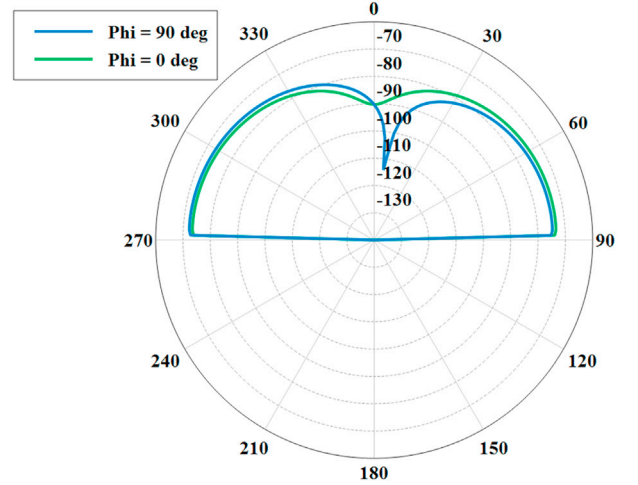


Fig. 5. Submillimeter wave RPA: Far-field radiation patterns due to excitation voltage of 2 V, 5 V.



(a) Antenna patterns at 0.1 THz operational frequency.

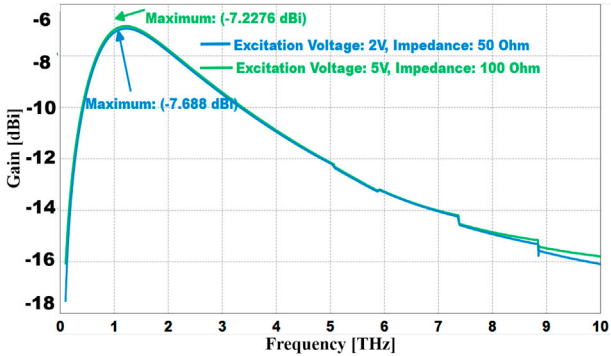
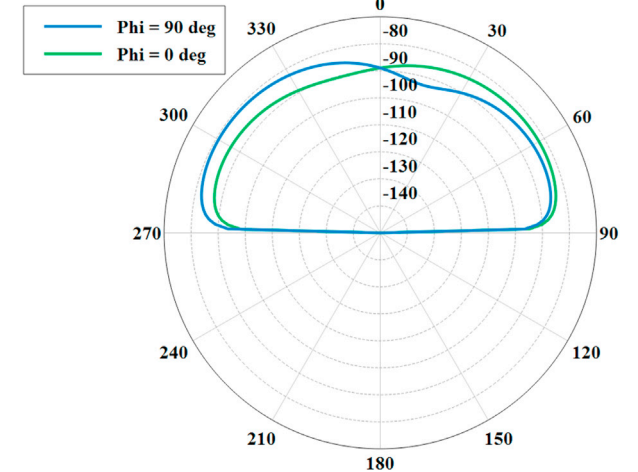


Fig. 6. Submillimeter wave RPA: Antenna gains due to excitation voltage of 2 V, 5 V.



(b) Antenna patterns at 10 THz resonant frequency.

$TE_{01\delta}$, and a higher substrate height of the submillimeter RPA, a dominant transverse electromagnetic mode for RPA, other than the fringing effect and electrical conductivity, the FEKO simulation takes too long. Therefore, we assume an excitation mode of $TE_{01\delta}$ for CDRA, a smaller substrate height of 2805 nm, an electromagnetic mode of TM_{010}^x with no fringing effect and perfect electrical conductivity.

Figs. 7 and 8 show the plots of the far-field radiation patterns of the millimeter wave RPA and submillimeter wave RPA when the excitation voltage is 1 V. The E-plane is defined by $-90^\circ \leq \theta \leq 90^\circ$ and $\phi = 90^\circ$, whereas the H-plane is defined by $-90^\circ \leq \theta \leq 90^\circ$ and $\phi = 0^\circ$. As explained in Ref. [5], the presence of the dielectric-covered ground plane modifies the reflection coefficient, which influences the magnitudes and phases of the plots in Figs. 7 and 8. For a dielectric-covered ground plane, the reflection coefficient for vertical polarization in the E-plane is nearly

Fig. 8. Submillimeter wave RPA: Far-field radiation patterns in E- and H- planes.

+1 for observation angles far away from grazing, and it begins to change rapidly near grazing and becomes -1 at the grazing angle $\theta = 90^\circ$ [21]. Similarly, the reflection coefficient also controls the pattern in the

H-plane. And for a dielectric-covered ground plane, it is -1 for all observation angles, but basically the H-plane pattern remains unaltered by the presence of the dielectric cover [21]. In Fig. 8a, the far-field antenna gain pattern of the submillimeter wave RPA in the E-plane at 0.1 THz has been observed to be slightly closer to -1 at the grazing angle $\theta = 90^\circ$, which is due to the magnitude of the reflection coefficient, $0.7 \leq |\Gamma| \leq 0.97$, as calculated in Table 1. Interestingly in Fig. 8b, at the resonant frequency 10 THz, the vertical polarization in the E-field, for all observation angles, has a reflection coefficient closer to $+1$. Horizontal polarization in the H-plane has a uniform reflection coefficient, closer to -1 at all observation angles for the resonant frequency of 10 THz. But at 0.1 THz, the horizontal polarization in the H-plane changes; and at a grazing angle, it has a reflection coefficient magnitude closer to $+1$. It can be seen that due to the usage of 5CB liquid crystal droplets as the dielectric substrate, the reflection coefficient of the dielectric-covered ground is closer to both -1 and $+1$. In Fig. 9, the bandwidth of the millimeter wave RPA is shown to be 0.347 GHz at -3 dB reflection, while Fig. 10 shows 4.39 THz at -3 dB reflection for the submillimeter wave RPA.

It has been observed that the bandwidth of a submillimeter wave antenna is more than 2500 times higher than that of the millimeter wave antenna at the same reflection of -3 dB. Also from Table 1, it is noted that the millimeter wave RPA has a maximum gain of 5.89 dBi in the E-field, whereas the submillimeter wave RPA has a low gain of -8.87 dBi; thus, it can be concluded that even when the bandwidth is wide, the path loss is high.

Since a massive MIMO antenna design can increase the overall antenna gain to compensate for path losses experienced by a single element antenna [7,8,9,10,11], section 4 discusses details regarding how it improves the behavior of a single element antenna. One very interesting observation is the high quality factor of the submillimeter wave CDRA, which signifies that even at the submillimeter wave, the CDRA can be used for designing effective submillimeter wave filters or submillimeter wave oscillators.

3.2. Cylindrical dielectric resonator antenna

The antenna patterns of the millimeter wave CDRA and the submillimeter wave CDRA have been plotted through POSTFEKO in Figs. 11 and 12, respectively.

Similar to what is shown in Table 1, the output parameters of both the millimeter wave CDRA and the submillimeter wave CDRA are tabulated in Table 2, which helps to compare the two.

It has been discussed previously how the reflection coefficient of a dielectric-covered ground plane changes the magnitude and phase of the far-field radiation pattern of the antenna. The magnitude of the reflection coefficient of the millimeter wave CDRA is $0.94 \leq |\Gamma| \leq 0.98$; hence, the antenna pattern in the E-plane is almost $+1$, thus showing no phase change at the grazing angle. On the other hand, the reflection coefficient

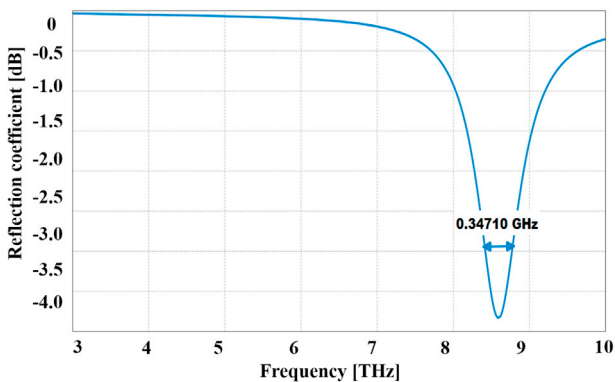


Fig. 9. Millimeter wave RPA: Bandwidth (ΔF) at -3 dB.

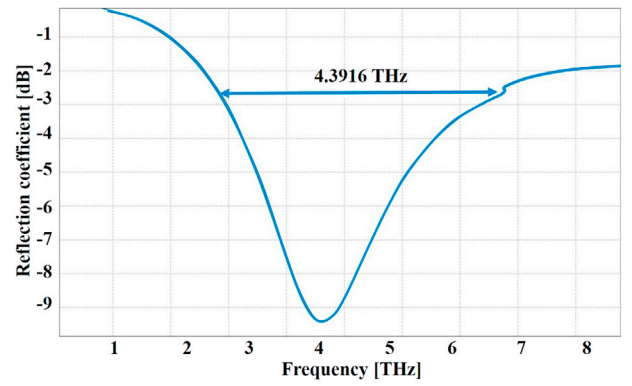


Fig. 10. Submillimeter wave RPA: Bandwidth (ΔF) at -3 dB.

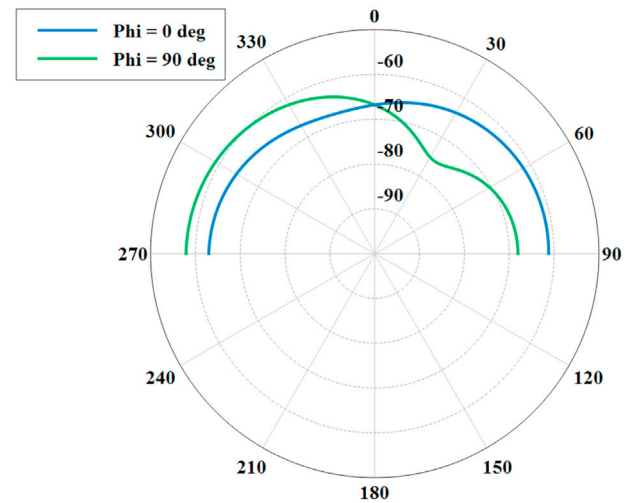


Fig. 11. Millimeter wave CDRA: Far-field radiation patterns in E- and H- plane.

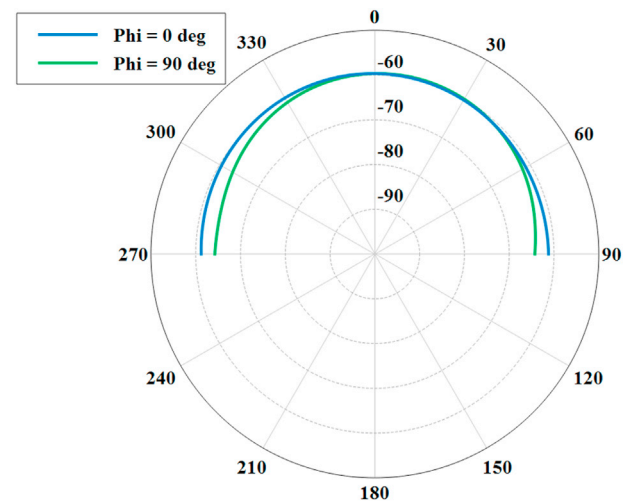


Fig. 12. Submillimeter wave CDRA: Far-field radiation patterns in E- and H- plane.

of the submillimeter wave CDRA is $0.975 \leq |\Gamma| \leq 0.99$; hence, as shown in Fig. 12, the antenna pattern in the E-plane is found to be a complete semicircle because the reflection coefficient now is approximately $+1$ at all observation angles with no change at the grazing angle. The antenna pattern in the H-plane remains unaltered in Fig. 11, but the phase and magnitude change in Fig. 10, which is also due to the variation in the

Table 2
FEKO simulated output parameters of CDRA.

Output parameter	Millimeter wave CDRA	Submillimeter wave CDRA
Free space wave number (k_0)	2.34	2.10
Wave number for the excitation mode ($k_0 a$)	1.20	1.08
Wavelength (λ)	2.99 cm	29,979 nm
Fractional bandwidth (BW)	0.22	0.24
Percentage bandwidth	22 percent	24 percent
Reflection coefficient magnitude ($ \Gamma $)	$0.94 \leq \Gamma \leq 0.98$	$0.975 \leq \Gamma \leq 0.99$
Quality factor (Q_c)	4.62	4.23
Maximum gain in E-field (G_0)	-57.92 dBi	-127.89 dBi
Total efficiency (ϵ_0)	70.05 percent	0 percent

reflection coefficient of the horizontal polarization in the H- plane. One very interesting observation that has been noted is the high-quality factor of the submillimeter wave CDRA, which signifies that even at the submillimeter wave, the CDRA can be used for designing effective submillimeter wave filters or submillimeter wave oscillators. The bandwidth of the submillimeter wave CDRA is wider than that of the millimeter wave CDRA.

The massive MIMO CDRA has also been designed and analyzed in this paper. The total efficiency of the submillimeter wave CDRA is found to be zero, as shown in Table 2, which is possibly because a single-probe feeding technique (instead of the commonly used co-axial-probe feeding method) has been used in the submillimeter wave CDRA design. A single-probe feeding model has been developed to process a faster simulation through FEKO. But at the same time, better designs or methods, as found in Ref. [22] or by conformal mapping as discussed in Ref. [23], need to be studied in detail for future experiments using the CDRA.

4. Massive MIMO antenna design and simulation

4.1. Rectangular patch antenna

The increasing demand for MIMO communication technology has motivated this work. In addition, this type of technology basically uses a very large number of service antennas (e.g., hundreds or thousands) that are operated fully coherently and adaptively [7,8,9,10,11]. Extra antennas help by focusing the transmission and reception of signal energy into ever-smaller regions of space. This can bring vast improvements in throughput and energy efficiency, particularly when combined with simultaneous scheduling of a large number of user terminals (e.g., tens or hundreds) as explained in Refs. [7,8,9,10,11]. Submillimeter wave massive MIMO technology can help to improve antenna efficiency by deploying an array of low-power, low-cost miniature antennas. The total efficiency of MIMO antennas designed in FEKO is found to be 100 percent, which is practically not possible. Once again, for maintaining simplicity in the design, the conductor is taken to be a perfect electric conductor; hence, there is no metallic loss, and the tangent loss of the dielectric material is assumed to be zero. Thus, the MIMO antenna system designed is taken to be a lossless system.

The results obtained from FEKO analysis are tabulated in Tables 3–5. It can be seen that an 8×8 submillimeter wave MIMO RPA has a gain of about -0.175 dBi, which is 4.43 dBi higher than that of the 4×4 submillimeter wave MIMO RPA, and 9.75 dBi higher than a 2×2 submillimeter wave MIMO RPA. On the other hand, the 8×8 mm wave MIMO RPA has a gain of about 24.38 dBi, which is 5.26 dBi higher than that of the 4×4 mm wave MIMO RPA, and 10.9 dBi higher than a 2×2 mm wave MIMO RPA.

Figs. 13 and 14 show the antenna far-field patterns of a 2×2 mm wave MIMO RPA and a 2×2 submillimeter wave MIMO RPA. Figs. 15 and 16 show the antenna patterns of a 4×4 mm wave MIMO RPA and a 4×4 submillimeter wave MIMO RPA, while Figs. 17 and 18 demonstrate

Table 3
MIMO RPA (2×2) antenna design specifications.

Parameter	Millimeter wave MIMO RPA	submillimeter wave MIMO RPA
Wavelength (λ)	124.91 mm	29,979 nm
Resonant frequency (f_0)	60 GHz	10 THz
Gain (G_0)	13.41 dBi	-9.93 dBi
Total efficiency (ϵ_0)	100 percent	100 percent

Table 4
MIMO RPA (4×4) antenna design specifications.

Parameter	Millimeter wave MIMO RPA	submillimeter wave MIMO RPA
Wavelength (λ)	124.91 mm	29,979 nm
Resonant frequency (f_0)	60 GHz	10 THz
Gain (G_0)	19.12 dBi	-4.45 dBi
Total efficiency (ϵ_0)	100 percent	100 percent

Table 5
MIMO RPA (8×8) antenna design specifications.

Parameter	Millimeter wave MIMO RPA	submillimeter wave MIMO RPA
Wavelength (λ)	124.91 mm	29,979 nm
Resonant frequency (f_0)	60 GHz	10 THz
Gain (G_0)	24.38 dBi	-0.175 dBi
Total efficiency (ϵ_0)	100 percent	100 percent

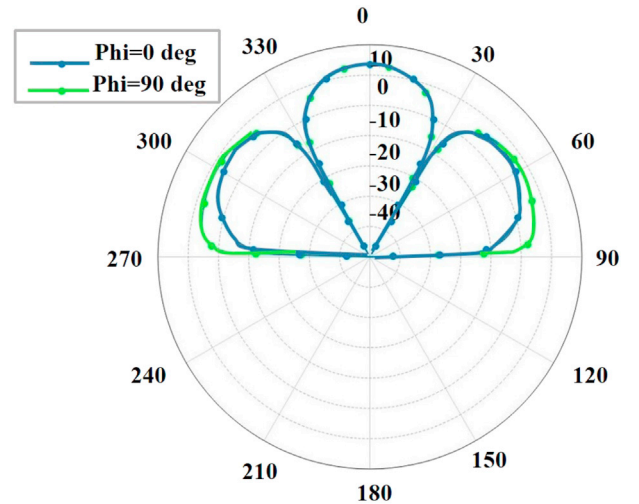


Fig. 13. 2×2 Millimeter wave MIMO RPA: Far-field radiation patterns in E- and H- planes.

the same for an 8×8 massive millimeter wave MIMO RPA and an 8×8 massive submillimeter wave MIMO RPA.

4.2. Cylindrical dielectric resonator antenna

Results obtained from FEKO simulation of the MIMO CDRA antenna design are tabulated in Tables 6–8. It can be seen that an 8×8 submillimeter wave MIMO CDRA has a very low gain of about -40 dBi, which is 6 dBi higher than that of the 4×4 submillimeter wave MIMO CDRA and 13 dBi higher than a 2×2 submillimeter wave MIMO CDRA. On the other hand, the 8×8 mm wave MIMO CDRA has a gain of about 5.59

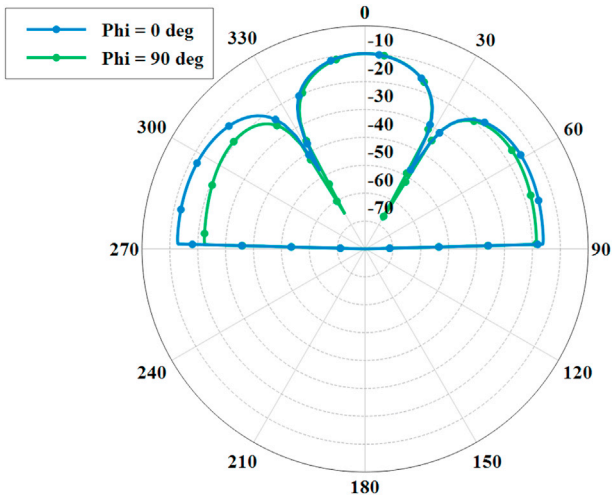


Fig. 14. 2×2 Submillimeter wave MIMO RPA: Far-field radiation patterns in E- and H- planes.

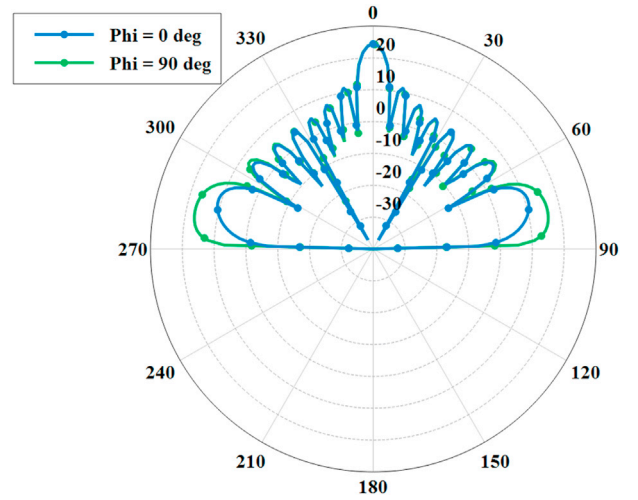


Fig. 17. 8×8 Millimeter wave MIMO RPA: Far-field radiation patterns in E- and H- planes.

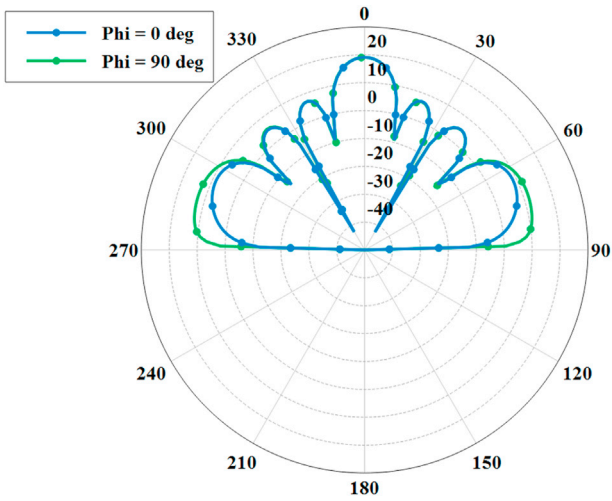


Fig. 15. 4×4 Millimeter wave MIMO RPA: Far-field radiation patterns in E- and H- planes.

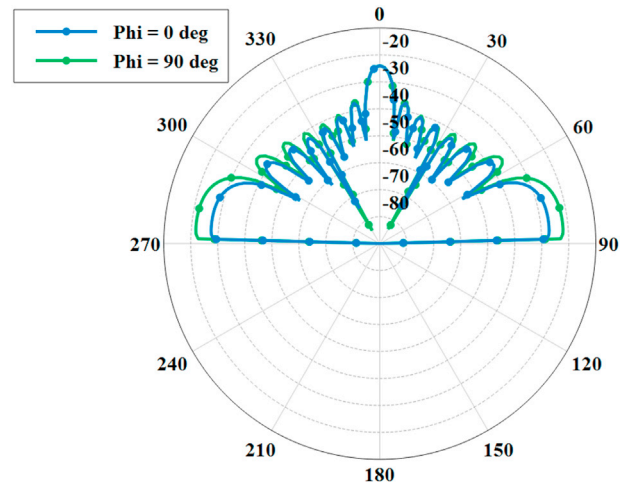


Fig. 18. 8×8 Submillimeter wave MIMO RPA: Far-field radiation patterns in E- and H- planes.

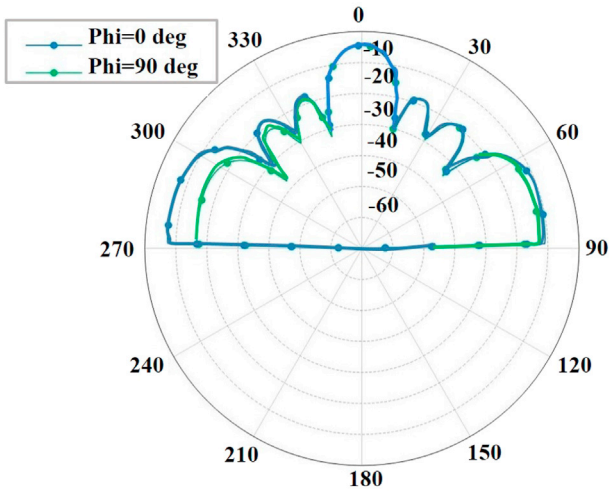


Fig. 16. 4×4 Submillimeter wave MIMO RPA: Far-field radiation patterns in E- and H- planes.

Table 6
MIMO CDRA (2×2) design specifications.

Parameter	Millimeter wave MIMO CDRA	Submillimeter wave MIMO CDRA
Wavelength (λ)	2.99 cm	29,979 nm
Resonant frequency (f_0)	60 GHz	10 THz
Gain (G_0)	-7.98 dBi	-53.79 dBi
Total efficiency (e_0)	100 percent	100 percent

Table 7
MIMO CDRA (4×4) design specifications.

Parameter	Millimeter wave MIMO CDRA	Submillimeter wave MIMO CDRA
Wavelength (λ)	2.99 cm	29,979 nm
Resonant frequency (f_0)	60 GHz	10 THz
Gain (G_0)	-0.73 dBi	-46.56 dBi
Total efficiency (e_0)	100 percent	100 percent

Table 8
MIMO CDRA (8 × 8) design specifications.

Parameter	Millimeter wave MIMO CDRA	Submillimeter-wave MIMO CDRA
Wavelength (λ)	2.99 cm	29,979 nm
Resonant frequency (f_0)	60 GHz	10 THz
Gain (G_0)	5.59 dBi	-40.77 dBi
Total efficiency (ϵ_0)	100 percent	100 percent

dBi, which is 4.86 dBi higher than that of the 4 × 4 mm wave MIMO CDRA and 13.5 dBi higher than that of the 2 × 2 mm wave MIMO CDRA. The MIMO CDRA antenna is also designed to be lossless for maintaining simplicity in the computation using FEKO.

Figs. 19 and 20 show the plots of the far-field antenna patterns of a 2 × 2 mm wave MIMO CDRA and a 2 × 2 submillimeter wave MIMO CDRA, respectively. The antenna far-field patterns of a 4 × 4 mm wave MIMO CDRA and a 4 × 4 submillimeter wave MIMO CDRA are shown in Figs. 21 and 22, respectively; and the antenna far-field patterns of an 8 × 8 massive millimeter wave MIMO CDRA and an 8 × 8 massive submillimeter wave MIMO CDRA are shown in Figs. 23 and 24, respectively.

The results above do not consider beamforming weight vectors when calculating the antenna radiation pattern. Since the array pattern of the antennas affects the beam formation to a large extent, a linear One-Dimensional (1D) antenna array as well as a planar nonlinear 2D antenna array are both included in the discussion. Once again due to space limitation, we limit our plots for 1D and 2D RPA antenna array only. The Array Factor (AF) for the linear 1D RPA antenna array pattern can be expressed as

$$AF(\phi, \phi_0) = \frac{w^H}{1 \times N} \times v[:, \phi] \quad (4)$$

In equation (4), N signifies the number of elements in the linear array, and K = 100,000 sampling points. Since the angle of incidence ϕ can vary between 0 and 180° when sampled at K sampling points, the steering vector matrix $v[:, \phi]$ can be expressed as

$$v_{N \times K}[:, \phi] = \begin{bmatrix} v[:, \phi_1] & v[:, \phi_2] & \dots & v[:, \phi_K] \end{bmatrix} \quad (5)$$

Where the steering vector $v[:, \phi_k]$ for $k = 1, \dots, K$ sampling points is obtained from the following equation

$$v(\phi) = e^{-j\frac{2\pi}{\lambda}d}, \quad (6)$$

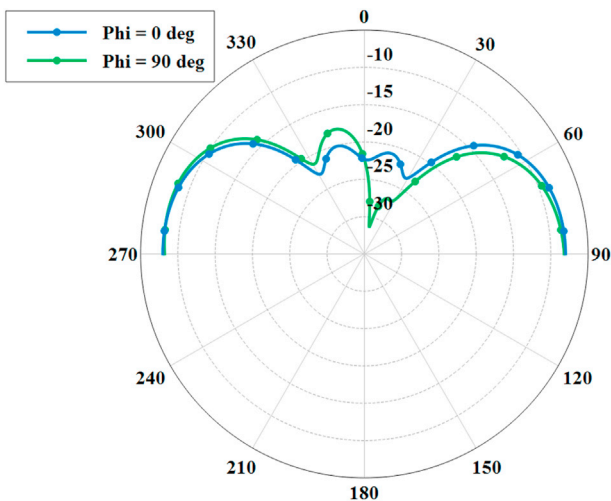


Fig. 19. 2 × 2 Millimeter wave MIMO CDRA: Far-field radiation patterns in E- and H- planes.

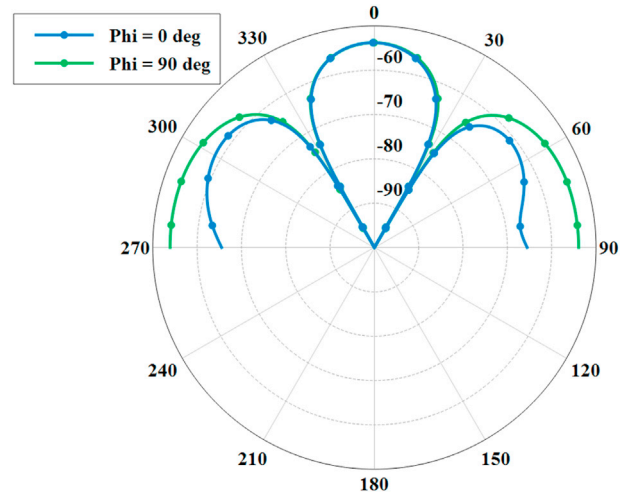


Fig. 20. 2 × 2 Submillimeter wave MIMO CDRA: Far-field radiation patterns in E- and H- planes.

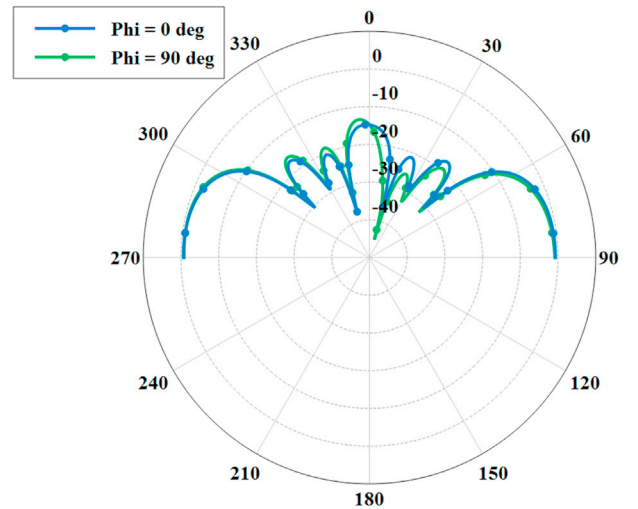


Fig. 21. 4 × 4 Millimeter wave MIMO CDRA: Far-field radiation patterns in E- and H- planes.

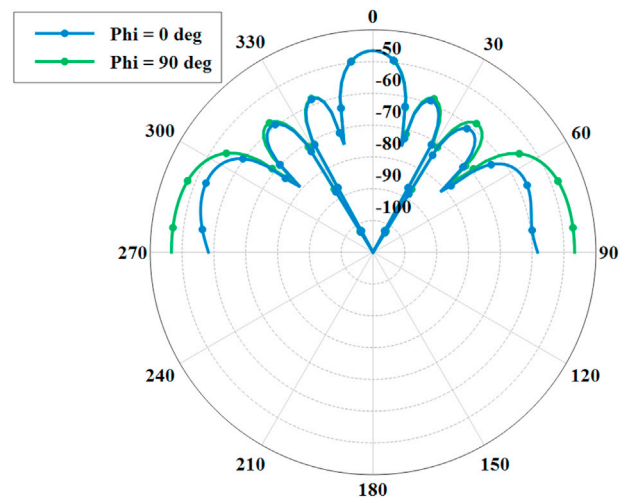


Fig. 22. 4 × 4 Submillimeter wave MIMO CDRA: Far-field radiation patterns in E- and H- planes.

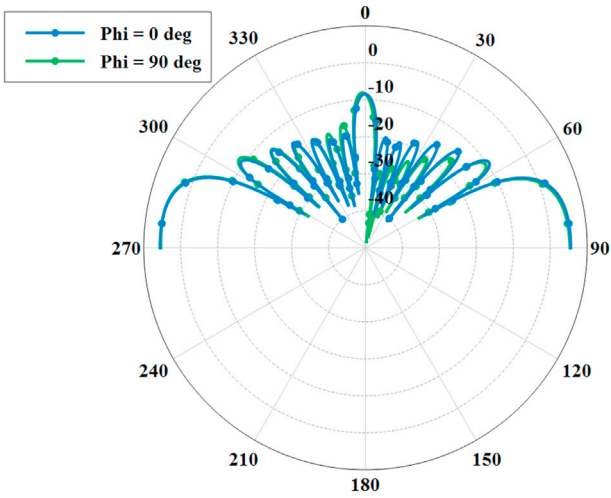


Fig. 23. 8 × 8 Millimeter wave MIMO CDRA: Far-field radiation patterns in E- and H- planes.

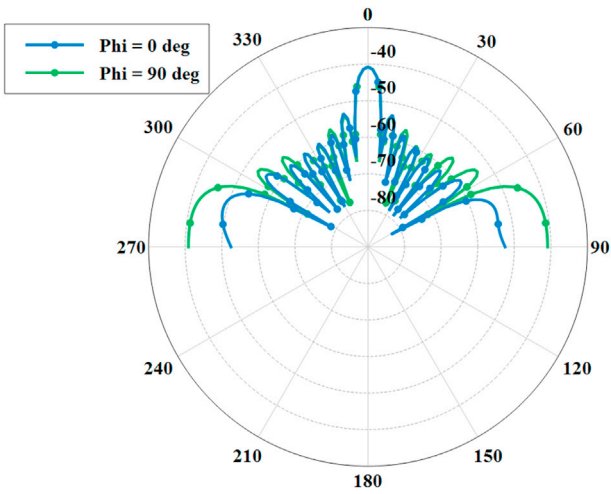


Fig. 24. 8 × 8 Submillimeter wave MIMO CDRA: Far-field radiation patterns in E- and H- planes.

where λ is the wavelength, and d is the distance of the antenna element from the reference point expressed as

$$d = (|\underline{e}_n|)(|\underline{r}_n - \underline{r}_1|)(|\cos\phi|). \quad (7)$$

r_n for $n = 1 \dots$, where N antenna elements are the coordinate points corresponding to each antenna element, while \underline{e} refers to the unit vectors in the direction of the coordinate axes. The weight vectors are expressed as the function of the steering angle ϕ_0 in the following equation:

$$\underline{w}_{N \times 1} = \frac{1}{N} e^{-j\frac{2\pi}{\lambda} (|\underline{e}_n|)(|\underline{r}_n - \underline{r}_1|)(|\cos\phi|)}. \quad (8)$$

When beamforming vectors are not associated, then we get antenna pattern similar to that shown in Fig. 25, which is obtained for a 1D array; whereas Fig. 26 represents a multiple beam formation with steering angles at 45° and -30° for a 1D array. A similar method can be applied for the 2D planar array. The beamforming weight vectors for the 2D planar array are expressed as a function of both azimuthal angle (ϕ) and elevation angle (θ) as

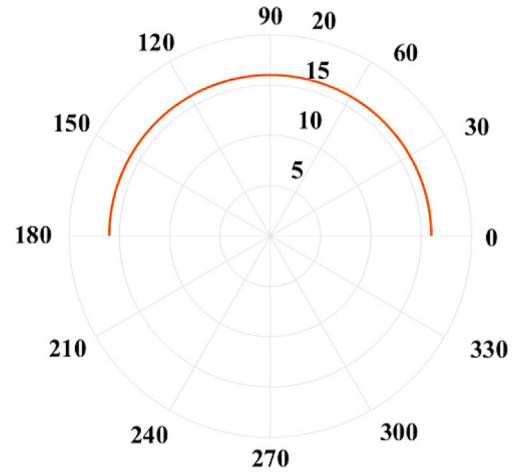


Fig. 25. Linear array (1D) antenna pattern without beamforming.

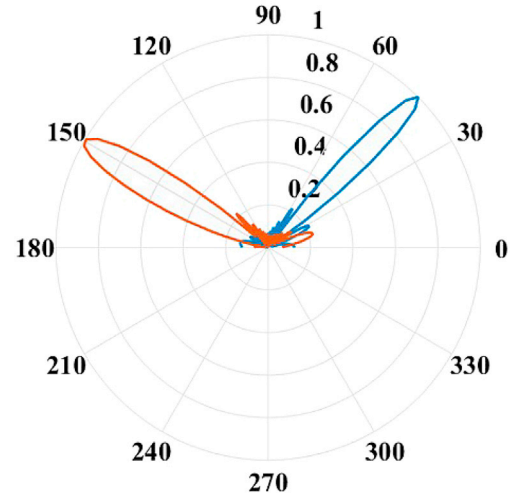


Fig. 26. Linear array (1D) antenna pattern with beamforming.

$$\underline{w}_{(N \times N) \times 1} = \frac{e^{-j\frac{2\pi}{\lambda} (|\underline{e}_{n-x} - \underline{e}_1|)(|\cos\theta_0 \sin\phi_0|)(|\underline{e}_{n-y} - \underline{e}_1|)(|\cos\theta_0 \cos\phi_0|)}}{N \times N}. \quad (9)$$

The array factor can be expressed as a function of θ , ϕ , θ_0 , and ϕ_0 as

$$\underline{AF}(\phi_0, \theta_0, \phi, \theta) = \underline{w}^H(\phi_0, \theta_0) \times v[\phi, \theta \leq 90^\circ], \quad (10)$$

where the steering vector matrix has each of its elements with a dimension of $(N \times N) \times 1$.

Fig. 27 shows a rectangular array 2D antenna pattern without beamforming.

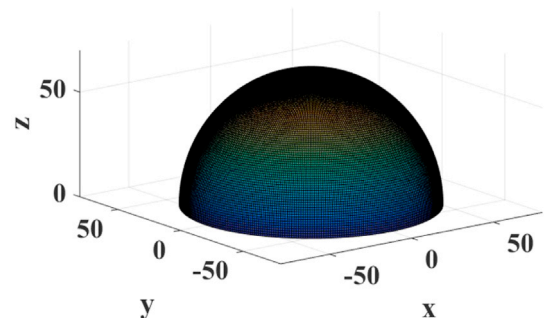


Fig. 27. Rectangular Array (2D) antenna pattern without beamforming.

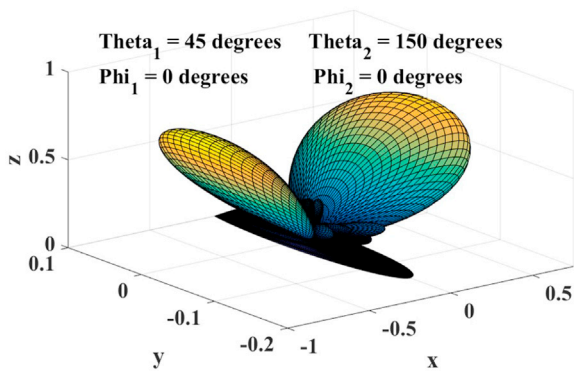


Fig. 28. Rectangular Array (2D) antenna pattern with beamforming.

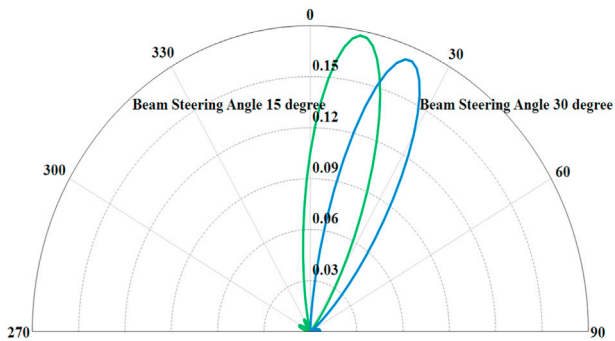


Fig. 29. 2×2 submillimeter wave MIMO RPA: Far-field radiation patterns in E- and H- planes with beamforming vectors.

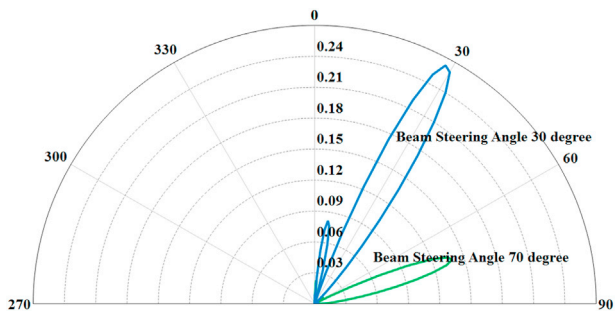


Fig. 30. 4×4 submillimeter wave MIMO RPA: Far-field radiation patterns in E- and H- planes with beamforming vectors.

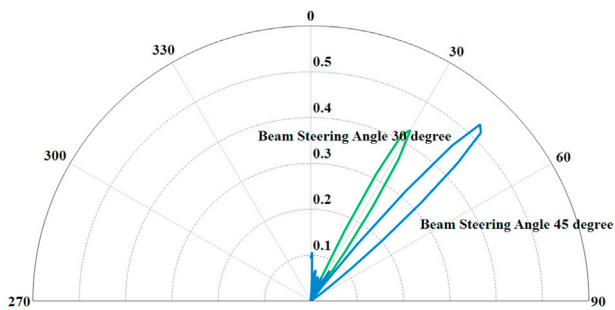


Fig. 31. 8×8 submillimeter wave MIMO RPA: Far-field radiation patterns in E- and H- planes with beamforming vectors.

beamforming, while Fig. 28 displays the rectangular array 2D antenna pattern with beamforming steered at angles -30° and 45° .

In Figs. 29–31, the far-field radiation patterns of 2×2 , 4×4 , and 8×8 submillimeter wave MIMO RPA can be seen. The beamforming weight vectors are applied to increase the antenna gain and reduce the path loss due to high frequency. When beamforming weight vectors are implemented, the antenna gain increases by 0.1633 dBi from -9.93 dBi (without beamforming vectors) with θ_0 at 30° for a 2×2 MIMO RPA, by 0.26 dBi from -4.45 dBi (without beamforming vectors) with θ_0 at 30° for a 4×4 MIMO RPA, and by 0.51 dBi from -0.175 dBi (without beamforming vectors) with θ_0 at 45° for a 8×8 MIMO RPA.

5. Conclusions

This paper studies, for the first time, a massive MIMO antenna design for the submillimeter wave while operating in the infrared region of the electromagnetic spectrum with a frequency ranging between 0.1 THz and 10 THz and analyzes its performance using FEKO software. This paper also applies the digital BF method to increase the antenna gain and to combat path loss due to high frequency range over the submillimeter wave frequency band.

In this paper, we have observed the BF gains of the massive MIMO antenna when the frequency increases from the millimeter wave to the submillimeter wave, and when the number of antennas increases from 4 to 64. As shown in Tables 3–5, the RPA antenna gain improvement of 10.97 dB occurs when the number of antennas is increased from 4 to 64 for the millimeter frequency, and the RPA antenna gain improvement of 9.755 dB occurs when the number of antennas is increased from 4 to 64 for the submillimeter frequency. Tables 6–8 show the CDRA antenna gain improvement when the number of antennas is increased from 4 to 64 for both the millimeter and submillimeter frequency ranges. It can also be seen that the bandwidth expands from 3.47×10^8 Hz to 4.39×10^{12} Hz when the frequency is increased from the millimeter wave to the submillimeter wave.

We have also discussed the practical scenario when the excitation voltage at the feeding point of the antenna varies. All of the designs in this paper involve computational electromagnetic principles. The practical development of these designed antennas and their testings follow standard antenna testing procedures as discussed in Ref. [24]. And this would be an effective way to deal with the challenges faced thus far in achieving better antenna performance.

Acknowledgement

This work is supported in part by the Asian Office of Aerospace Research and Development (AOARD) AFRL under Grant FA2386-14-1-0026. The views and conclusions contained herein are those of the authors and should not be interpreted as necessarily representing the official policies or endorsements, either expressed or implied, of the AFRL or the U.S. Government.

References

- [1] M. Giordani, A. Zanella, M. Zorzi, Millimeter wave communication in vehicular networks: challenges and opportunities, in: Modern Circuits and Systems Technologies (MOCAST), 2017 6th International Conference on, IEEE, 2017, pp. 1–6.
- [2] A. Rashid, A possible method of generating submillimeter wave (correspondence), IEEE Trans. Microw. Theory Tech. 12 (3) (1964), 384–384.
- [3] J.M. Jornet, I.F. Akyildiz, Graphene-based nano-antennas for electromagnetic nanocommunications in the terahertz band, in: Proceedings of the Fourth European Conference on Antennas and Propagation (EuCAP), IEEE, 2010, pp. 1–5, 2010.
- [4] F. Ding, Z. Wang, S. He, V.M. Shalae, A.V. Kildishev, Broadband high-efficiency half-wave plate: a supercell-based plasmonic metasurface approach, ACS Nano 9 (4) (2015) 4111–4119.
- [5] A. Koval'chuk, L. Dolgov, O. Yaroshchuk, Dielectric studies of dispersions of carbon nanotubes in liquid crystal 5CB, Semicond. Phys. Quantum Electron. Optoelectron. 11 (4) (2008) 337–341.
- [6] J. Prost, The Physics of Liquid Crystals, vol. 83, Oxford University Press, 1995.
- [7] E.G. Larsson, O. Edfors, F. Tufvesson, T.L. Marzetta, Massive MIMO for next generation wireless systems, IEEE Commun. Mag. 52 (2) (2014) 186–195.

- [8] M. Wu, B. Yin, G. Wang, C. Dick, J.R. Cavallaro, C. Studer, Large-scale MIMO detection for 3GPP LTE: algorithms and FPGA implementations, *IEEE J. Select. Topics Signal Proces.* 8 (5) (2014) 916–929.
- [9] X. Gao, F. Tufvesson, O. Edfors, F. Rusek, Measured propagation characteristics for very-large MIMO at 2.6 GHz, in: *Conference Record of the Forty Sixth Asilomar Conference on Signals, Systems and Computers (ASILOMAR)*, IEEE, 2012, pp. 295–299, 2012.
- [10] Z. Xiang, M. Tao, X. Wang, Massive MIMO multicasting in noncooperative cellular networks, *IEEE J. Sel. Area. Commun.* 32 (6) (2014) 1180–1193.
- [11] G. Yang, C.K. Ho, R. Zhang, Y.L. Guan, Throughput optimization for massive MIMO systems powered by wireless energy transfer, *IEEE J. Sel. Area. Commun.* 33 (8) (2015) 1640–1650.
- [12] C.A. Balanis, *Advanced Engineering Electromagnetics*, John Wiley & Sons, 1999.
- [13] A.B. Constantine, et al., *Antenna Theory: Analysis and Design, MICROSTRIP ANTENNAS*, third ed., John Wiley & Sons, 2005.
- [14] A. Petosa, *Dielectric Resonator Antenna Handbook*, Artech House Publishers, 2007.
- [15] F. Yang, Y. Rahmat-Samii, *Electromagnetic Band-Gap Structures in Antenna Engineering (The Cambridge RF and Microwave Engineering Series)*, Cambridge University Press, 2008.
- [16] R.K. Mongia, P. Bhartia, Dielectric resonator antennas: a review and general design relations for resonant frequency and bandwidth, *Int. J. Microw. Millim. Wave Comput. Aided Eng.* 4 (3) (1994) 230–247.
- [17] A. Tarasov, K. Titov, On the use of the Cole-Cole equations in spectral induced polarization, *Geophys. J. Int.* 195 (1) (2013) 352–356.
- [18] N.Y. Canli, Ö. Yasa, C. Yorur, B.B. Eran, F. Yakuphanoglu, Dielectric anisotropy and dielectric relaxation dynamics in chiral and non-chiral salicylaldehyde nematic crystal composites, *Optoelectron. Adv. Mater.-Rapid Commun.* 4 (1) (2010) 86–92.
- [19] F. Salman, R. Khalil, H. Hazaa, Dielectric studies and Cole-Cole plot analysis of silver-ion conducting glasses, *Adv. J. Phys. Sc* 3 (1) (2014) 1–9.
- [20] J. Carr, G. Hippiusley, *Practical Antenna Handbook 5/e*, McGraw-Hill/TAB Electronics, 2011.
- [21] D.B. Davidson, I.P. Theron, U. Jakobus, F.M. Landstorfer, F.J. Meyer, J. Mostert, J.J. Van Tonder, Recent progress on the antenna simulation program FEKO, in: *Proceedings of the 1998 South African Symposium on Communications and Signal Processing (COMSIG)*, IEEE, 1998, pp. 427–430.
- [22] A. Helaly, A. Sebak, Radiation conductance and pattern of array antenna on a non-conformal dielectric-coated elliptic cylinder, *WSEAS Trans. Commun.* 11 (2008) 1091–1101.
- [23] F. Sun, S. He, Optical surface transformation: changing the optical surface by homogeneous optic-null medium at will, *Sci. Rep.* 5 (2015) 16032.
- [24] A.S. Committee, et al., *IEEE Standard Test Procedures for Antennas, ANSI/IEEE Std, 1949–1979*, p. 1979.